



Cite this: *Environ. Sci.: Processes Impacts*, 2019, 21, 242

# Characterization and implications of solids associated with hydraulic fracturing flowback and produced water from the Duvernay Formation, Alberta, Canada†

Shannon L. Flynn,<sup>a</sup> Konstantin von Gunten,<sup>b</sup> Tyler Warchola,<sup>b</sup> Katherine Snihur,<sup>b</sup> Tori Z. Forbes,<sup>c</sup> Greg G. Goss,<sup>d</sup> Murray K. Gingras,<sup>b</sup> Kurt O. Konhauser<sup>b</sup> and Daniel S. Alessi<sup>b</sup>

Public concern is heightened around flowback and produced water (FPW) generated by the hydraulic fracturing process. FPW is a complex mix of organic and inorganic solutes derived from both the injected hydraulic fracturing fluid and interactions with the subsurface lithology. Few studies to date have systematically investigated the composition of FPW or its individual components. Here, we provide the first systematic characterization of the composition of the solids associated with FPW by analyzing samples from three wells drilled into the Duvernay Formation in Alberta, Canada. The FPW initially returned to the surface with high total dissolved solids (greater than 170 000 mg L<sup>-1</sup>) and enriched with Fe(II), silica, sulfate, barium, and strontium. The solids form two distinct phases once the FPW reached the surface: (1) silica-enriched Fe(III) oxyhydroxides, and (2) a barite–celestine solid solution. We hypothesize that the precipitation of the amorphous silica-enriched Fe(III) oxyhydroxide is a two-step process, where first the silica precipitates as a function of the cooling of the FPW from elevated subsurface temperatures to ambient surface temperatures. Next, the silica acts as a template for the precipitation of Fe(III) oxyhydroxide as the diffusion of oxygen into the subsurface causes oxidation of aqueous Fe(II). The barite–celestine solid solution precipitates solely as a function of cooling. Elevated dissolved Fe concentrations in FPW and modeled saturation indices from five North American shale plays (Marcellus, Fayetteville, Barnett, Bakken, and Denver–Julesburg) indicate that solids similar to those found in Duvernay FPW, specifically Fe(III) oxyhydroxides, barite and quartz, are likely to occur. With the solids known to carry a significant portion of FPW's toxicity and organic contaminant load, the development of new treatment technologies, such as the oxidation of the Fe(II) in FPW, may increase FPW reuse and reduce the environmental risk posed by FPW.

Received 2nd September 2018  
Accepted 6th December 2018

DOI: 10.1039/c8em00404h

rsc.li/espi

## Environmental significance

Annually, hydraulic fracturing generates millions of litres of FPW. Understanding the composition of FPW is critical for determining the toxicity and risks associated with unintentional releases into aquifers and for the development of cost effective treatment techniques. In the first comprehensive study of FPW associated solids, our results show that the associated solids are composed of two distinct phases: silica-enriched Fe(III) oxyhydroxides and a barite–celestine solid solution. The FPW also contains high amounts of Fe(II), which through aeration becomes oxidized to form additional Fe(III) oxyhydroxides. To reduce the aqueous toxicity of FPW, large-scale aeration has the potential to be a new treatment technique to remove organic contaminants and heavy metals from FPW, increase water reuse, and reduce transportation risks.

<sup>a</sup>School of Natural and Environmental Sciences, Newcastle University, Newcastle upon Tyne, NE1 7RU, UK. E-mail: shannon.flynn@ncl.ac.uk

<sup>b</sup>Department of Earth and Atmospheric Sciences, University of Alberta, Edmonton, AB T6G 2E3, Canada

<sup>c</sup>Department of Chemistry, University of Iowa, Iowa City, IA, 52242, USA

<sup>d</sup>Department of Biological Sciences, University of Alberta, Edmonton, AB T6G 2E3, Canada

† Electronic supplementary information (ESI) available. See DOI: 10.1039/c8em00404h

## 1 Introduction

Hydraulic fracturing for oil and gas extraction has generated a range of environmental concerns including air pollution,<sup>2</sup> induced seismicity,<sup>3–5</sup> fresh water allocations,<sup>6–8</sup> drinking water contamination,<sup>9,10</sup> and human health risks.<sup>11–13</sup> While there has been substantial public concern on the potential for fluids related to hydraulic fracturing migrating to the shallow subsurface and contaminating groundwater, the most likely

routes for groundwater contamination are the loss of wellbore integrity or surface spills during the handling and transport of hydraulic fracturing fluid (HFF) or flowback and produced waters (FPW).<sup>9,14–18</sup>

Much of our current understanding of the composition of FPW comes from just a few locations, namely the Marcellus Formation (Northeast USA),<sup>19–21</sup> Julesburg basin (Colorado, USA),<sup>22,23</sup> Duvernay Formation (Alberta, Canada),<sup>1</sup> and Horn River Formation (British Columbia, Canada).<sup>24</sup> Generally, FPW has been found to contain high total dissolved solids (TDS), ranging from 10 000 to over 300 000 mg L<sup>-1</sup> depending on the formation, fracturing process, and time. The TDS is largely composed of Na and Cl, with elevated concentrations of Ca, Fe, Mg, and Sr.<sup>20–24</sup> Trace elements, such as Se, As, Ba,<sup>19</sup> and naturally occurring radioactive materials (NORMs),<sup>25,26</sup> have also been documented in FPW.

The organic chemical composition of FPW is also complex. FPW is composed not only of the hydrocarbons naturally present in the target geologic formation, but also HFF chemicals and the compounds that form as a product of secondary reactions when HFF is exposed to elevated subsurface temperatures and pressures.<sup>1,27</sup> As FPW can contain numerous combinations of the thousands of chemicals known to have been used in hydraulic fracturing fluids alone,<sup>13</sup> targeted analysis can be difficult. To date, a variety of compounds have been either identified or quantified in FPW, including volatile organic compounds (*e.g.*, benzene, toluene, ethylbenzene, and xylene),<sup>27–29</sup> polymers (*e.g.*, polyethylene glycols and polypropylene glycols),<sup>30–32</sup> biocides (*e.g.*, glutaraldehyde and alkyl dimethyl benzyl ammonium chloride: Ferrer and Thurman, 2015), surfactants (*e.g.*, dimethylamines, cocamidopropyl and its derivatives),<sup>33</sup> and reaction byproducts (*e.g.*, halogenated methanes and acetones, chloromethyls, delayed acids, and organophosphates).<sup>1,27</sup>

FPW compositional studies have focused the analysis primarily on the fraction that passes through a membrane (0.2 or 0.45  $\mu\text{m}$ ), *i.e.*, the dissolved phase. With the exception of a few filtration studies,<sup>34–37</sup> such as Phan *et al.*<sup>38</sup> who examined the composition of colloidal fractions that passed through 0.45  $\mu\text{m}$  pore filters, the associated solid and colloidal fractions that do not pass through the filters have been largely ignored. This is problematic because in previously studied contaminated aquifers, colloidal fractions are a major vector for the transport for contaminants, such as uranium,<sup>39,40</sup> plutonium,<sup>41,42</sup> and polycyclic aromatic hydrocarbons (PAHs).<sup>43,44</sup> Indeed, recent work has demonstrated strong links between the FPW solids, PAHs and environmental toxicity.<sup>1,45,46</sup> Specifically, He *et al.*<sup>1</sup> showed that zebrafish (*Danio rerio*) embryos exposed to unfiltered FPW samples had approximately double the ethoxyresorufin-*O*-deethylase (EROD) activity compared to those exposed to the corresponding filtered samples. Additionally, the 96 h LC<sub>50</sub> concentration for samples containing solids was approximately 50% lower than the corresponding samples without solids. Further, He *et al.*<sup>45</sup> found a significant increase in EROD activity and thiobarbituric acid reactive substances in gill, kidney and liver tissues of juvenile rainbow trout (*Oncorhynchus mykiss*) when FPW solids were present. The exact mechanisms by which

the solids cause the increased toxicity has yet to be determined, including whether the toxicity is derived primarily from the solids themselves or the associated organic compounds.

In this study, we have characterized the chemical composition and mineralogy of FPW associated solids from the Duvernay Formation. The Duvernay Formation is a Devonian-aged formation composed of silt-sized quartz, mica, K-feldspar, and plagioclase; the clay-size fraction is dominantly quartz and calcite with subordinate clay illite/smectite and less abundant kaolinite in descending order of their relative abundance<sup>47,48</sup> (for more information, a full description of the geologic context is provided in the ESI†). Using the FPW data we model the saturation indices for the minerals identified in the characterization of the solids and then discuss the mechanisms underpinning their formation with a comparison to the potential for secondary mineral formation in five other North American shale plays. Analysis of bulk chemistry of aqueous and solid phases capture on 0.2  $\mu\text{m}$  membranes were conducted, and particle morphology and spot elemental and mineralogy of the solids were determined using spectroscopy. 0.2  $\mu\text{m}$  membranes were selected as it has been suggested that 0.2 or 0.45  $\mu\text{m}$  are the most commonly used pore sizes used microfiltration for FPW reuse.<sup>49</sup> The strong correlations observed between toxicity, oxidative stress, endocrine disruption, and the FPW solids<sup>1,45</sup> indicates the importance of characterizing these solids. Insights into their composition and formation will improve the handling, treatment, and disposal technologies to mitigate risks.

## 2 Methods

### 2.1 Flowback samples

Samples of FPW from three hydraulically fractured wells located near Fox Creek, Alberta, Canada in the Devonian-aged Duvernay Formation were acquired from Encana Corporation. All samples were collected after the oil and gas separator into polypropylene buckets. Sample 1 (S1) was collected 7 days after the initiation of the flowback and collected in August 2014, which was previously examined for aqueous toxicity and characterized in He *et al.*<sup>1,45</sup> Sample 2 (S2) collected 10 days after the initiation of the flowback and collected in November 2015.<sup>47</sup> Sample 3 (S3) from 24 h after the initiation of the flowback and collected in October 2016. Upon arrival the pH of each fluid was measured using a Mettler Toledo Easy Five dual pH meter, which was calibrated using a 3 point calibration method using buffers pH 4.01, 7.00, 10.01. The buffers were not matched to the ionic strength of the FPW and there for should be viewed as an estimate. A portion of S3 was further treated by vigorously bubbling it with air for 4 hours, subsequently referred to as S3\_Ox.

### 2.2 X-ray diffraction spectroscopy

Two samples of Duvernay shale collected as drill cuttings from 700 m apart along the horizontal bore of the hydraulic fractured well from which S3 were acquired were analyzed for their bulk mineral composition (Fig. SI.1†). Samples were soaked for 1 h in with Optima™ grade *n*-hexane at a ratio of 10 mL solvent to

0.5 g sample to remove residual drilling fluid organic compounds. The cuttings were recovered by centrifugation and then the remaining solvent was allowed to evaporate before analysis. Bulk mineralogy was determined using X-ray diffraction (XRD) using a Rigaku Ultima IV. A  $^{60}\text{Co}$  radiation source and a scan rate of  $2^\circ \text{ min}^{-1}$  with a step size of  $0.02^\circ$  were used, spectra was then fit using JADE 9 software and ICDD (International Centre for Diffraction Data) and ICSD (Inorganic Crystal Structure Database).

### 2.3 Digestions

Samples of FPW solids for digestion were prepared using a method similar to He *et al.*<sup>1</sup> Each of the three FPW samples were thoroughly shaken before being passed through a nylon membrane filter with a nominal pore size of  $0.2 \mu\text{m}$ . The solids retained by the filter were then rinsed with 18 M $\Omega$  ultrapure water while still on the filter, then covered and air dried for 48 h at room temperature.

The bulk elemental composition of the FPW solids was determined by alkaline fusion digestion performed in triplicate using a method similar to that described by GBC Scientific Equipment.<sup>51</sup> Alkaline fusion digestions were chosen over hydrofluoric acid digests due to the potential for the loss of Si from the evaporation of  $\text{SiF}_4$  and  $\text{SiF}_6$  and the precipitation of Al, Fe, Sr fluoride minerals in hydrofluoric acid digestions. Additionally, von Gunten *et al.*<sup>52</sup> found alkaline fusion and hydrofluoric digestions to yield comparable results for total digestions. For each, 1.5 g of NaOH was melted in a nickel crucible over a Bunsen burner, and then 0.1 g of sample was added to the melt with 0.5 g of  $\text{Na}_2\text{O}_2$  and an additional 0.5 g of NaOH. The crucibles were then covered with nickel covers and heated for an additional 5 minutes. After cooling, the crucibles were rinsed with 6 M HCl before being placed into a polypropylene beaker along with the lid. Aliquots of 6 M HCl were added until all the remaining particles dissolved (approximately 20–30 mL), the final the volume was adjusted to 100 mL with 18 M $\Omega$  ultrapure water. Solutions were diluted 10-fold with a mixture containing 2%  $\text{HNO}_3$  and 0.5% HCl prior to analysis by ICP-MS/MS (see Section 2.3.1). Metal recoveries were verified using STSD-3 reference material (CANMET Mining and Mineral Sciences Laboratories), which was digested in parallel to the samples.

### 2.4 Aqueous analysis

The aqueous phase of samples S1 and S2 were previously analyzed and reported in He *et al.*<sup>1</sup> and Blewett *et al.*,<sup>50</sup> respectively. For S3 and all aqueous phase analyses, the samples were vigorously shaken before an aliquot was removed and filtered through a  $0.2 \mu\text{m}$  nylon membrane filter into polypropylene ICP tubes. The filtrate was then used for all subsequent analyses.

**2.4.1 ICP-MS analysis.** The aqueous phase of S3 and digestion solutions from S1-3 and S3\_Ox were analyzed using an Agilent 8800 ICP-MS/MS. S3 was diluted with 18 M $\Omega$  ultrapure water with a dilution factor (DF) of 850 for Na analysis and 85 for all other elements. After dilution, S3 was acidified with 12  $\mu\text{L}$  of trace metal grade nitric acid per 10 mL of sample and all

blanks were prepared in a similar manner with the sample fraction being replaced with 18 M $\Omega$  ultrapure water. During analysis, the RF power was set to 1550 W and the reflected power was 18 W. Samples were aspirated with a micromist nebulizer and nickel/copper cones were used. MS/MS mode was used for sample analysis to acquire greater mass resolution, and the gas collision/reaction cell was utilized with either He,  $\text{O}_2$  or  $\text{H}_2$  gas depending on the element. To account for instrumental drift, a standard solution of 0.5 ppm indium (In) was added to each sample utilizing an inline addition system.

**2.4.2 Ion chromatography.** Ion chromatography was used to determine the chloride ( $\text{Cl}^-$ ) and sulfate ( $\text{SO}_4^{2-}$ ) concentrations of S3. Filtered samples were diluted 1 : 2000 with 18 M $\Omega$  ultrapure water and then analyzed using a Dionex ion chromatography DX 600 with a 4 mm analytical column (AS9-HC), guard column (AG9-HC), and a 4 mm ASRS Ultra suppressor.

**2.4.3 Total organic carbon and total nitrogen analysis.** Total organic carbon (TOC) and total nitrogen (TN) were determined using a Shimadzu model TOC-V-CHS/CSN TOC analyzer. TOC was measured as nonpurgeable organic carbon. TN was measured as  $\text{NO}_2$  after the sample was combusted.

**2.4.4 Alkalinity measurements.** The alkalinity was determined for S1–S3 upon arrival from the field through an endpoint titration to pH 4.5 in which 50 mL of FPW was titrated with 0.1 M HCl using a Metrohm Titrand 905. The milliequivalents (meq) of acid required to lower the pH was used to calculate the total alkalinity of the sample as ppm of  $\text{CO}_3^{2-}$ .

**2.4.5 Iron(II) analysis.** The concentration of Fe(II) was determined using the ferrozine assay as described in Porsch and Kappler.<sup>53</sup> In summary, 400  $\mu\text{L}$  of 1 M HCl was added to 100  $\mu\text{L}$  of each sample, followed by an additional 500  $\mu\text{L}$  of 0.1% by weight ferrozine. Samples were allowed to react for 5 min in the dark before spectrophotometric analysis at 562 nm using an Evolution 60S UV-Vis Spectrophotometer (Thermo Scientific). External calibration standards were prepared using Fe(II) ammonium sulfate to cover a range of 0.05–55 ppm Fe(II). Samples were diluted as needed to be within the calibration range.

### 2.5 Microscopy

**2.5.1 Scanning electron microscopy (SEM).** A portion of the solids from each sample collected for digestion were set aside for imaging. Samples were then added to SEM tabs using carbon tape by dabbing the tab and tape onto the filters. Imaging was performed using a Zeiss Sigma 300 VP-FESEM in variable pressure mode with energy dispersive X-ray spectroscopy (EDS) with dual silicon detectors, each with 60 mm<sup>2</sup> of surface area and having a resolution of 123 eV. For better resolution of particle morphologies, the samples were subsequently carbon coated using a Nanotek SEMprep 2 sputter coater before reanalysis in high resolution mode under high vacuum.

**2.5.2 Transmission electron microscopy (TEM) with EDS and selected area electron diffraction (SAED).** The solids from S1 were suspended in 18 M $\Omega$  ultrapure water at a concentration of approximately 1 mg L<sup>-1</sup>. The suspension was then drop cast

onto a 400 mesh carbon-coated copper grid (Pacific Grid Tech), then air dried. Imaging was conducted using a FEI Titan 80-300 TEM operating at 80 and 200 kV with point-to-point resolution of 0.19 nm and a single tilt sample holder capable of rotating from  $-30$  to  $30^\circ$ . Elemental analysis was performed using an Oxford INCA 30 mm<sup>2</sup> LN<sub>2</sub> EDS detector with a 130 eV energy resolution, along with SAED.

### 2.5.3 Scanning transmission electron microscopy (STEM).

A 1 g L<sup>-1</sup> suspension of the solids from S1 was placed on ultra-thin carbon-coated copper grids. Excess water was removed with paper filters and the residual was evaporated under a stream of N<sub>2</sub> gas. TEM analysis was then conducted using a JEOL JEM-ARM200CF Atomic Resolution S/TEM at the NanoFAB facility at the University of Alberta. Scanning transmission electron microscopy (STEM) coupled to energy-dispersive X-ray spectroscopy (EDX) was done to localize particles of interest and to generate elemental maps. Transmission electron microscopy (TEM) and selected area electron diffraction (SAED) was then performed on selected particles with a camera length of 60 cm. SAED patterns were analyzed following the manufacturer's instructions. Specifically, the distance (in pixel) of diffraction peaks to the center beam and d-spacing was measured using the Gatan Microscopy Suite Software.

## 3 Results and discussion

### 3.1 Aqueous chemistry

The TDS was found to range from 171 000 to 243 000 ppm, with the primarily solutes for all three samples comprising Na and Cl (85–97%). While the TDS is known to generally increase with time after FPW has started,<sup>19,20,22,23</sup> the TDS of S3 was composed of the highest percentage of Na and Cl (97%) and was within 6% of S2 (91%) even though S2 was collected 9 days later. This indicates that variables, such as shut-in time and the use of recycled FPW for the mixing of HFF, effects the temporal variation of FPW's composition. The higher fractions of Na and Cl in sample S3 was likely due to approximately 10% of the makeup fluid for the HFF used to fracture well S3 being recycled FPW from other wells. Other major elements (those greater than 0.5%) were Ca, K, and Sr, descending order of their relative concentration. Trace elements (those less than 0.5%) Br, Li, Mg, Mn, B, Zn, Ba, and S were detected in every sample (Table 1). Aqueous Si was only detected in S1, which is not unexpected given the low solubility of Si minerals at room temperature, including amorphous silica.<sup>54,55</sup> The presence of Ba in the FPW is likely related to the dissolution of barite or desorption from aluminosilicate clays as has been suggested by Renock *et al.*<sup>56</sup> into the fracturing fluids. Sr in the FPW is likely linked to a combination of inclusions in carbonates and barite, in addition to desorption from clays much like Ba. Further investigation and leaching studies would be required to full understand the distributions of Ba and Sr and their subsequent mobilization. Silica could come from a variety of sources including the dissolution of quartz in the formation or the sand used as proppants. The elevated subsurface temperatures are likely not great enough on their own to explain the aqueous Si concentrations, and likely it, in combination with the complexation of

**Table 1** Summary of the aqueous chemistry for the three samples analyzed in this study. Reported concentrations and detection limits (DL) are in ppm unless otherwise noted. BDL denotes below detection limit and NM indicates the parameter was not measured for the corresponding sample. In brackets, the relative standard deviation for each analysis is presented as the percent within one deviation<sup>a</sup>

	DL	S1*	S2 <sup>#</sup>	S3
TDS		243 000	183 000	171 000
pH		4.78	5.86	5.51
Alkalinity (as CaCO <sub>3</sub> )	NM	2.25	14.3	54.4
T (C°) at collection		60	NM	38
TOC	0.46	212	737	294
TN	0.27	498	425	410
Cl	0.04	136 000	107 000	112 000
Na	0.33	70 000	59 500	54 300
Ca	1.13	11 800	6500	8630
K	1.47	2570	2160	1930
Sr	0.049	1470	931	904
Br	0.24	276	297	242
Fe	0.23	22	1.19	151
S	0.18	64.5	66.9	78.3
Si	0.37	7.9	BDL	BDL
Ba	0.00022	5.85	7.28	24.1
SO <sub>4</sub> <sup>2-</sup>	0.2	48.7	BDL	BDL
Li	0.00038	54.6	51.3	41.3
B	0.021	71.6	96	79.1
Mg	0.090	111	706	738
Mn	0.00090	15.8	7.32	15.1
Ni	0.0055	BDL	BDL	BDL
Cu	0.01	BDL	BDL	BDL
Zn	0.018	4.4	1.24	0.561
As	0.0050	BDL	BDL	BDL
Cd	0.00013	BDL	BDL	BDL
Pb	0.00014	0.06	BDL	BDL

<sup>a</sup> The chemistry of S1 and S2 were previously reported in \*He *et al.*;<sup>1</sup> <sup>#</sup>Blewett *et al.*,<sup>50</sup> respectively, with the new analyses being conducted for alkalinity and total sulfur for both and Pb, Cu, and Si for S2.

Si with organic matter, plays a critical role in the dissolution of the quartz as has been observed in room temperature systems.<sup>57,58</sup>

The total organic carbon (TOC) concentration was the highest in S2 at 737 ppm, which was more than double S3 at 294 ppm and S1 at 212 ppm. As observed by He *et al.*<sup>1</sup> for S1, the total nitrogen (TN) was higher than TOC for S3 at 410 ppm; however, this was not observed in S2 at 425 ppm (Table 1). The relatively lower TOC than TN is likely due to most organic compounds in the samples being associated with an immiscible phase that floated on top of the aqueous samples, and which was, therefore, not collected by the autosampler during analysis.<sup>1</sup>

The presence and persistence of aqueous Fe(II) found in S3 (254 ppm) and S1 (35.7 ppm) indicates that either weak or transient oxidizing conditions exist in the subsurface through the introduction of HFF. It is unclear whether all the Fe(II) mobilized during fracturing returns to the surface or only a portion that is the residual remains after the precipitation of Fe(III) minerals that result from the subsurface oxidation of the mobilized Fe(II), as suggested by Jew *et al.*<sup>59</sup> The fact that Fe(II) has been found in the FPW suggests that the reducing

conditions were reestablished in the subsurface post fracturing. The most likely source of Fe is pyrite as experiments with Marcellus shale materials under hydraulic fracturing temperatures and pressures have found a correlation between the mobilization of Fe and the initial pyrite content of the shale used in the experiment.<sup>49</sup> Additionally, leaching experiments on Horn River Formation shales (British Columbia, Canada) with DI water in equilibrium with atmospheric oxygen found the oxidation of pyrite released sulfate and Fe(II).<sup>60</sup> Elevated levels of Fe, presumably Fe(II), is a widespread observation in the FPW of numerous formations in addition to the Duvernay Formation, including the Marcellus Formation (0.3–747 mg L<sup>-1</sup>),<sup>20,21,61</sup> Barnett Formation (50–300 ppm),<sup>71</sup> Bakken Formation (0.7–96 ppm)<sup>62</sup> and Bowland Formation (36.6–137 mg L<sup>-1</sup>).<sup>64</sup> The aeration of S3 resulted in a 75.6% decrease in aqueous Fe(II), and in terms of color, from transparent yellow to turbid orange (Fig. SI.2†). Collectively, the decrease in aqueous Fe(II), change in color and increase in turbidity are consistent with the precipitation Fe(III) oxyhydroxides, such as ferrihydrite (Fe(OH)<sub>3</sub>), as has been previously hypothesized to account for losses of aqueous Fe during the handling of Marcellus FPW by Phan *et al.*<sup>38</sup> and Tasker *et al.*<sup>65</sup>

### 3.2 XRD analysis

Both samples of drill cuttings from well 3 were found to contain quartz, calcite, muscovite, and aragonite (Fig. SI.3†). Sample A was found to contain sanidine, while sample B had kaolinite. The results of the bulk analysis are in generally in agreement with the literature for the composition of Duvernay Formation. The shales and argillites of the Duvernay have been shown to be primarily composed of quartz, mica, feldspar, plagioclase, calcite, and illite/smectite with less amounts of kaolinite.<sup>47,48</sup> There due to the heterogeneity within the formation it is not unsurprising that pyrite and barite might not found in the two samples which can be locally common.<sup>48,66</sup>

### 3.3 Solids analysis

The chemical composition of the solids for each sample were dominated by Fe and Si, with lesser amounts of S, Ca, Sr, and Ba (Fig. 1 and SI.4† for mg kg<sup>-1</sup>). Trace amounts (less than 100 mM) of Al, K, Mg, P, Mn, and Zn were detected, however, not in every sample (Table SI.1†). The largest variations between samples was their ratios of Si to Fe, not their elemental composition. S1 was predominately Fe-rich, with the next most abundant element being Si (3351 mM kg<sup>-1</sup>); S, Ba, Ca, and Sr were the only other elements greater than 99 mM kg<sup>-1</sup>. In contrast, S2 had an excess of Si to Fe 5842 to 1630 mM kg<sup>-1</sup> respectively. Additionally, S2 had the highest amounts of S (778 mM kg<sup>-1</sup>), and Sr (717 mM kg<sup>-1</sup>). S3 also had a Si : Fe ratio greater than 1 (1.34) and had the highest ratios of Ca and Ba, 0.21 and 0.16, respectively. The Sr + Ba : S molar ratio for all samples was approximately 1 and 0.89, 0.98, and 0.94 for S1, S2, and S3, respectively. In contrast, the relative abundances of Ba and Sr do vary: S1 and S3 have a relative excess of Ba to Sr, 1.37 and 1.42, while S3 contained a low Ba to Sr ratio, 0.07.

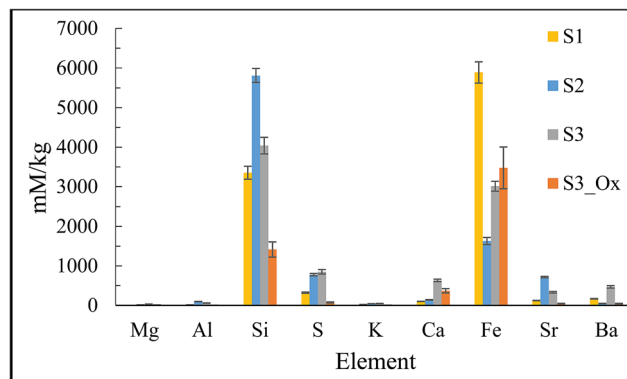


Fig. 1 Elemental profile of FPW solids as determined through alkaline fusion digestion, in with the error bars representing  $\pm 1$  standard deviation.

Aerating S3 (S3\_Ox) resulted in the decline of the relative ratio of Si/Fe from an excess of Si to an excess of Fe (Si/Fe = 0.41). The ratios of Si, Ba, Ca, and Sr to Fe also declined. Aeration was effective in the removal of dissolved Fe(II) and the concomitant generation of Fe(III) precipitates. The Ba/S ratio between samples S3 and S3\_Ox were similar at 0.55 and 0.59, respectively, while the ratio of Sr/S showed a Sr enrichment in S3\_Ox (0.61) compared to S3 (0.39). The removal of Sr during aeration is also evident in the relative abundance of Ba/Sr which shifted from 1.41 (excess Ba) to 0.98. The removal of Sr from solution during aeration suggests its adsorption or incorporation during the precipitation of the Fe(III) oxyhydroxides. The incorporation of Sr into iron oxides has previously been observed during ferrihydrite ripening to goethite.<sup>67</sup>

### 3.4 Morphological and chemical characterization

The backscatter SEM images (Fig. 2A, C, E, and G) show the solids had two particle morphologies: (1) globular neoformed aggregates, and (2) stellated clusters. For both particle types, the strong C signals observed were attributed to the carbon coating used to prepare the samples and the carbon-based tape used to affix samples to the aluminum tabs, and the strong O signal primarily to O associated with the mineral oxides that comprise the solids. We cannot exclude the possibility that a portion of the C and O signal was related to organic compounds associated with the sample, however, with the carbon tape it is impossible to quantify what portion that may be. Investigating whether there is significant insoluble organic carbon associated with the FPW solids will need to be investigated in the future. For the purposes of this study, C and O have been excluded from the discussion that follows. The EDS spectrum (grey bars) of S1's globular, neoformed aggregates have an approximate composition in molar percent of: Si (2.19%) and Fe (5.13%) (Fig. 2B). The neoformed aggregates in S2 and S3 showed similar elemental profiles (Fig. 2D and H). However, for S3\_Ox, an increase in the relative molar percent of Fe was observed (Fig. 2F and H). While the ratio of Fe to Si varied between samples and EDS spots, neither element was found independent of the other. These observations suggest that the neoformed aggregates are

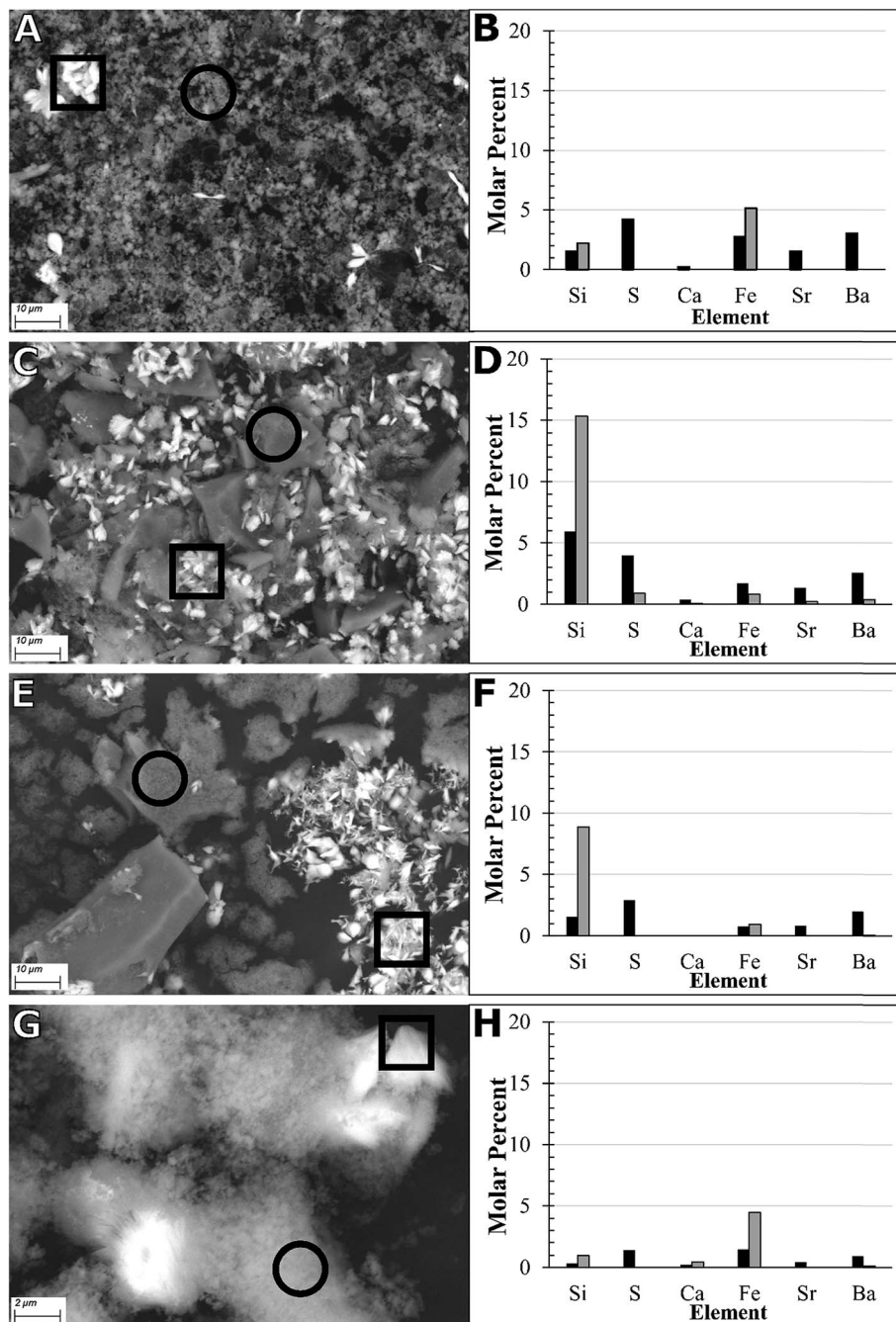


Fig. 2 SEM images in backscatter mode and elemental distribution determined by EDS of samples S1 (A and B), S2 (C and D), S3 (E and F), and S3\_Ox (G and H). In each SEM image the square and circle represent the location from which the EDS spectra was acquired and correspond to the black and white bars in the corresponding elemental distributions as molar percent, respectively.

discrete Fe/Si phases, representative of a silica-enriched Fe(III) oxyhydroxide.

Representative EDS spectra targeting the stellated clusters in S1 (Fig. 2B) show that they are composed of S (4.19%), Sr (1.54%), Ba (3.02%), Si (1.54%), and Fe (2.78%), with a close association between S, Ba and Sr stellated clusters from S2, S3, and S3\_Ox exhibited similar elemental profiles (Fig. 2D, F, and H). This correlation was not observed in the neoformed aggregates. Fe and Si were not observed in every spectrum with S, Ba, and Sr. We attributed the low presence of Fe and Si in the EDS

spectra as an artifact of the large EDS spot size, which resulted in the EDS beam also contacting part of the neoformed aggregates silica-enriched Fe(III) oxyhydroxide. The consistent elemental profile of stellated clusters indicates that they are singular phase composed of Sr, Ba, and S, with a Sr + Ba : S molar ratio of approximately 1. This is consistent with a sulfate mineral such as barite or celestine.

Across all three samples, the neoformed aggregates of the untreated samples showed a similar spherical particle morphology and size (~200 nm) (Fig. 3A–C). Aerating S3

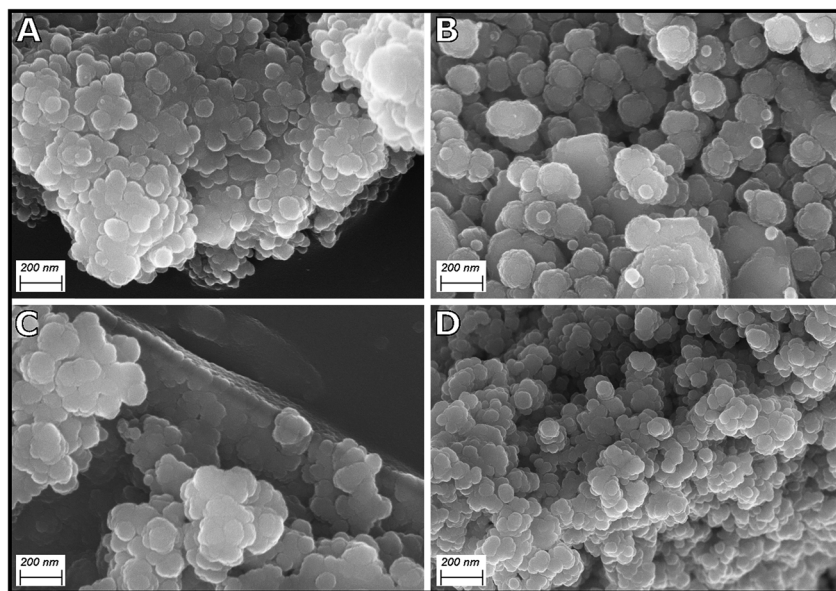


Fig. 3 High resolution SEM images of carbon coated samples showing the morphology of Fe/Si globular neoformed aggregates associated solids: (A) S1, (B) S2, (C) S3, and (D) S3\_Ox.

generated additional neoformed aggregates of a similar size and morphology to those found in the untreated samples (Fig. 3D). A comparison of S3 and S3\_Ox revealed that S3 had plates of granular aggregates composed of 200 nm spherical particles with a few aggregates associated with the surfaces, while S3\_Ox has numerous colloidal aggregates on the surfaces (Fig. 3A and B).

HRTEM with EDS and SAED was further used to probe the composition and mineralogy the Fe/Si phase. HRTEM images of S1 reveal a lack of order amongst the neoformed aggregates, with no visible edge steps (Fig. 4A and B). The elemental composition was dominated by Fe and Si (Fig. 4D). The SAED pattern generated from the Fe/Si aggregates (Fig. 4C) showed no apparent diffraction pattern, indicating a lack of crystallinity consistent with an amorphous silica enriched Fe(III) oxyhydroxide phase. STEM elemental maps of the solids from sample 1 show a strong association between Fe, Si and O (Fig. SI.5A–C†). The Si appears to have a higher abundance at the core of the particle with the Fe aggregating on the Si core. The elemental map of the Sr + Ba : S phase show that a higher concentration of S compared to Sr or Ba and that all three elements are concentrated in the particle (Fig. SI.6A–D†).

### 3.5 Modeled saturation indices

The saturation indices of each sample were calculated as a function of temperature, from 10 to 120 °C. This represents the approximate range of temperatures that FPW would encounter as it returns from the elevated subsurface temperatures, approximately 115 °C for the Duvernay Formation,<sup>68</sup> and equilibrates at the surface. The thermodynamic modeling was performed in PHREEQC<sup>69</sup> utilizing the Pitzer database due to the high ionic strength of the FPW samples 4.11, 3.24 and 3.31 M for S1, S2, and S3, respectively. The Pitzer database included barite (BaSO<sub>4</sub>), celestine (SrSO<sub>4</sub>), quartz (SiO<sub>2</sub>), and

amorphous silica (SiO<sub>2(am)</sub>). To model the SI, the measured concentrations from S1, S2, and S3 of all elements found to be greater than 100 ppm (Na, Cl, Ca, K, Sr, Br, and Mg) and Fe, S, Ba, and Si were utilized, with the pH set at that measured for each respective sample. For the purpose of this model all S from the total dissolved S measurement was assumed to be sulfate (SO<sub>4</sub><sup>2-</sup>) during modeling. S speciation in flowback is known to include thiosulfate and hydrogen sulfide, however, they have been found to be relatively minor components totaling less than 10% the sulfate concentration.<sup>70</sup> To begin, the sensitivity of the saturation indices to changes in pH was examined the models were run as pH sweeps from 3–10. The saturation indices for barite and celestine were found to not be sensitive to pH across the pH range examined (Fig. SI.7A and B†), while the saturation indices of silica was found to decrease exponentially above pH 8, well above the pH of the FPW samples examined (Fig. SI.8†). Additionally, the models were examined for to determine whether the evolution of CO<sub>2</sub> may have occurred during the cooling process, which could have influenced changes in FPW pH, however, across the temperature range examined the saturation indices for CO<sub>2</sub> was well below 0 (Fig. SI.9†).

S1, S2, and S3 were found to be supersaturated with respect to barite at room temperature (20 °C). The saturation indices show a distinct trend of increasing with decreasing temperature, which indicates that it is more thermodynamically favorable to form a solid phase as the solution cools (Fig. 5A). S3 had the highest equilibrium temperature, approximately 90 °C, which may be attributed to its being the freshest sample and the process of precipitation being kinetically slow. In contrast, all three samples were found to be undersaturated with respect to celestine with saturation indices ranging from –0.28 to –0.66 across the entire temperature range examined (Fig. 5B). As the models were performed using elemental analysis collected on solutions that had been fully cooled, this does not mean that

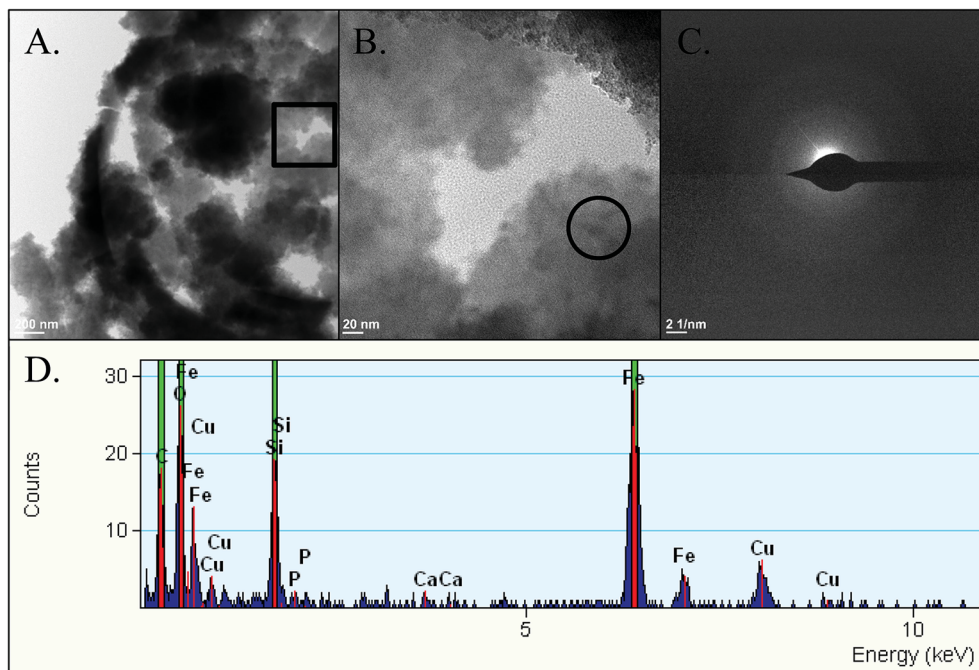


Fig. 4 TEM analysis of solids of S1. (A) A wide image in which the square represents the location of the close-up image in panel (B). (B) is a close-up image in which the circle represents the approximate location of the SAED spectra presented in panel (C) and EDS spectra presented in panel (D).

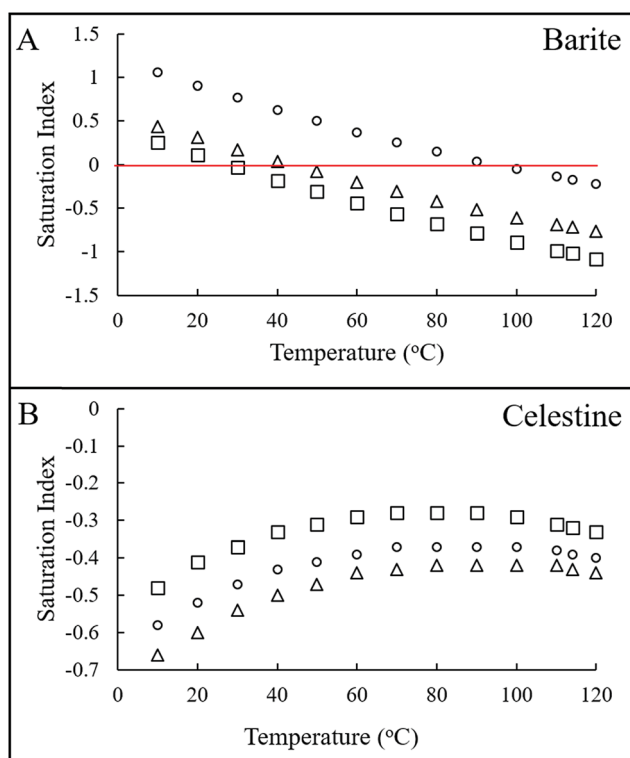


Fig. 5 Saturation indices of hypothesized minerals present in Duvernay FPW modeled using the element data as a function of temperature (A) respect to barite, and (B) celestine, with S1, S2, and S3 represented by (□), (△), and (○), respectively.

the solution was not previously supersaturated with respect to celestine. It is more plausible that the Sr concentration was initially drawn down during the cooling by the precipitation of celestine. The continued precipitation of barite after the celestine reached equilibrium likely drew down the sulfate concentration and potentially the Sr concentration through incorporation to reflect the measured undersaturated concentrations. Interestingly, S2 had the lowest saturation indices and the lowest Ba/Sr ratio in the sediment (0.070).

While Si was found in solids of all three samples, Si was only above the detection limit in the aqueous phase of S1. For S1 we modelled the saturation indices for this sample with respect to the two silicate minerals quartz and amorphous silica. At room temperature, S1 was supersaturated with respect to quartz but not  $\text{SiO}_{2(\text{am})}$ . S1 was supersaturated with respect to quartz below 60 °C; in contrast the lowest saturation indices for  $\text{SiO}_{2(\text{am})}$  was  $-0.67$  (Fig. 6). Furthermore, we modeled each sample in equilibrium with respect to either barite and celestine or quartz and  $\text{SiO}_{2(\text{am})}$  to determine how the measured Si, Ba, Sr, and sulfate concentrations compared to the modeled equilibrium concentrations. Regarding the silicate minerals, S1 had an excess of Si with respect to quartz below 80 °C, respectively. In contrast, S1 was below the modeled Si equilibrium concentration with respect to  $\text{SiO}_{2(\text{am})}$  across the entire temperature range, but by less than 1 mM when the temperature was below 30 °C (Fig. SI.11†). Even if we assume samples S2 and S3 had no measurable Si in solution, they too are still only below the equilibrium concentration of Si by less than one mM for quartz across the entire temperature range, and by less than one mM when the temperature is at or below 20 °C for  $\text{SiO}_{2(\text{am})}$ .

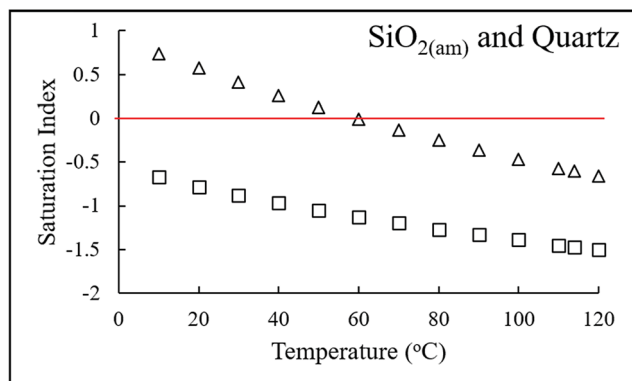


Fig. 6 Saturation indices of potential silicate minerals present in Duvernay FPW modeled using the element data from S1 as a function of cooling for  $\text{SiO}_{2(\text{am})}$  ( $\square$ ), and quartz ( $\triangle$ ).

For S1, the system was found to be supersaturated with respect to sulfate across the modeled temperature range and to have an excess of Ba when the temperature was below 50 °C. Across the examined temperature range, Sr was below the equilibrium concentration by 2.26–3.04 mM (Fig. SI.10A†). Similarly, S3 had an excess of sulfate and Ba across the entire temperature range and Sr was below the equilibrium concentration by 2.62–3.59 mM (Fig. SI.10C†). In contrast, S2 was below the equilibrium concentrations of sulfate and Sr across the entire temperature range, by 56.4 and 20.1 mM respectively, while below 70 °C there was an excess of Ba (Fig. SI.10B†).

### 3.6 Multi-basin comparison

Publicly available FPW chemistry data for the Fayetteville (4 samples),<sup>70</sup> Marcellus (day 14 flowback median from 7 wells, average of 95 well, 2 composite samples of days),<sup>20,21,34</sup> Bakken (median of 4 wells from day 10–12),<sup>62</sup> Barnett (median from day 10–12 from 4 wells)<sup>63</sup> and Denver-Julesburg (DJ) Formations (4 wells)<sup>73</sup> were modeled for using the same PHREEQC model developed for the Duvernay Formation (full modeling parameters are shown in Table SI.2†). While each basin is expected to have heterogeneity, these models offer a first pass determine how similar the FPW solids are between shale basins and how widely applicable treatment options would be. In the case of absent pH data for the Fayetteville and Marcellus, the pH was assumed to be 7 as the models only showed a pH dependence above pH 8.

For barite, below 90 °C the precipitation was found to be favorable (saturation indices greater than 1) for FPW from the Marcellus, Bakken, Barnett and DJ formations for all sample where the sulfate concentration was reported (Fig. 7A). Below 30 °C this also included the Duvernay. The Fayetteville was the only formation for which the precipitation of barite was not thermodynamically favorable across the temperature range. In contrast the precipitation of celestine was favorable for 3 out of the 4 Marcellus samples across the entire temperature range examined (Fig. 7B). For all other basins, the formation of celestine was not favorable at any temperature. However, as

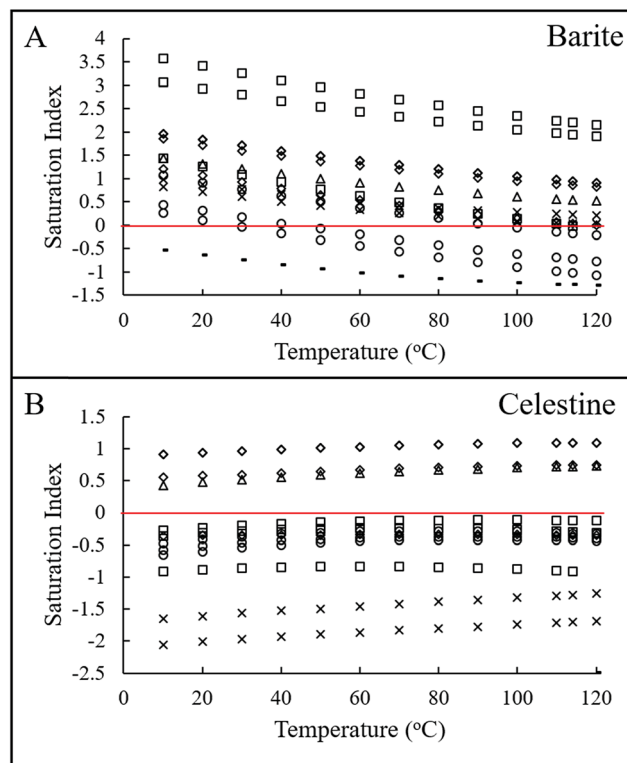


Fig. 7 A cross basin comparison of saturation indices of FPW for (A) barite and (B) celestine as a function of temperature for the Duvernay, Marcellus, Barnett, Bakken, Denver-Julesburg, and Fayetteville ( $\circ$ ), ( $\square$ ), ( $\triangle$ ), ( $\diamond$ ), ( $\times$ ) and ( $-$ ), respectively.

observed in this study for the Duvernay, this does not preclude the possibility of Sr incorporation into barite or the formation of a solid solution of Sr/Ba( $\text{SO}_4$ ). For all basins save the Fayetteville the saturation indices for celestine was greater than  $-1$ , meaning it is close to being in equilibrium with celestine.

Saturation indices for quartz and  $\text{SiO}_{2(\text{am})}$  was only modeled, in addition to the Duvernay Formation, for Fayetteville and DJ as dissolved silica data was not available for the Bakken, Marcellus and Barnett.  $\text{SiO}_{2(\text{am})}$  was found to have a saturation indices greater than 0 only for 1 out of 5 of the Fayetteville FPW samples (Fig. 8A). In contrast the formation of quartz was found to be favorable in all three basins with dissolved Si data below 50 °C (Fig. 8B). Additionally, for the Marcellus while the absence of dissolved silica data precluded the modeling of saturation indices silica has been identified through SEM EDS analysis of solids fouling filters used for Marcellus FPW.<sup>34</sup> This indicates the absence of dissolved silica data or when it is found to be below the detection limit would not mean that the formation of quartz would not be favorable.

Additionally, appreciable concentrations dissolved Fe were reported in each of the basins Fayetteville (1–13 ppm),<sup>71</sup> Marcellus (40.8–747 ppm),<sup>20,21,34</sup> Bakken (0.7–96 ppm),<sup>62</sup> Barnett (12.1–93.8 ppm)<sup>72</sup> and DJ (2.71–19).<sup>73</sup> This indicates that the precipitation of insoluble Fe(III) oxyhydroxides is likely across more than the Duvernay and Marcellus Formations where it has already been observed<sup>138,65</sup>.

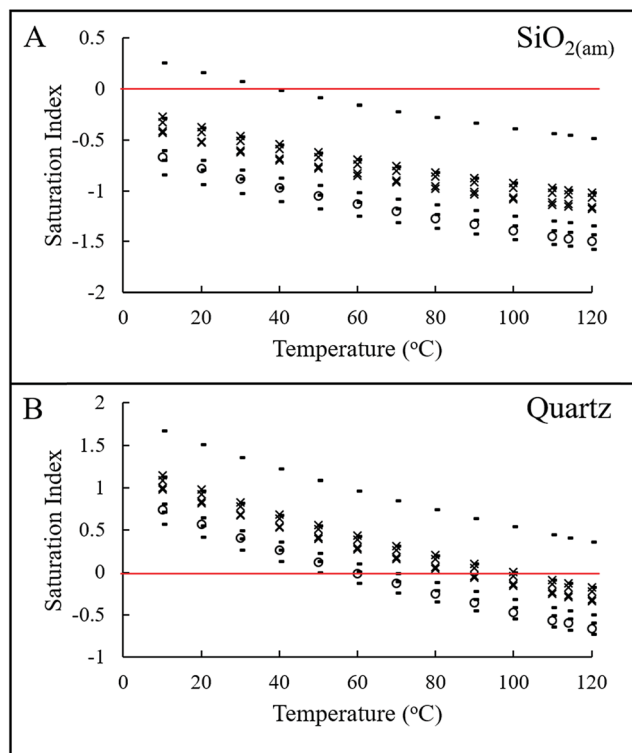


Fig. 8 A cross basin comparison of saturation indices of FPW for (A)  $\text{SiO}_{2(\text{am})}$  and (B) quartz as a function of temperature for the Duvernay, Bakken, Denver-Julesburg, and Fayetteville (O), ( $\Delta$ ), (x) and (-), respectively.

### 3.7 Mechanisms of formation

The amorphous Fe/Si phase likely formed through a two-step process. First, the FPW returned to the surface from the target formation with an elevated temperature ( $\sim 115$  °C for the Duvernay,<sup>68</sup> 82 °C for the Fayetteville,<sup>74</sup> 104 °C for the Marcellus,<sup>75</sup> 71–116 °C for the Bakken,<sup>76</sup> 93 °C for the Barnett,<sup>74</sup> and 116 °C for the DJ Formation<sup>77</sup> and enriched in dissolved Si relative to surface temperatures.<sup>54,55</sup> As the FPW cooled, Si became increasingly supersaturated with respect to amorphous silica. Second, with the increasing oxygen solubility and diffusion associated with cooling, the dissolved Fe(II) oxidized to Fe(III), and through subsequent hydrolysis formed insoluble Fe(III) oxyhydroxides. The Fe(II), and at least a portion of the sulfate, was probably derived from the oxidation of pyrite ( $\text{FeS}_2$ ) by oxygenated fracturing fluid. In this process sulfide in pyrite in the formation oxidized to sulfate, consuming the oxygen in the fracturing fluid releasing sulfate and Fe(II) into solution.<sup>69</sup> The subsurface conditions rapidly return to anoxic after the oxygen is consumed through sulfide oxidation, which prevents the Fe(II) from also oxidizing to Fe(III). The Fe(III) oxyhydroxides are always closely associated with amorphous silica, an unsurprising observation given that Fe(III) oxyhydroxides have a high sorption capacity for dissolved silica.<sup>78,79</sup> However, in our study the evidence points towards the adsorption and templating of Fe(III) oxyhydroxides onto amorphous silica to be the process by which this phase formed. Additionally, the diffusion of oxygen may be limited by thin surface oil films on the FPW, as were

observed in our samples. Nonetheless, the residual Fe(II) can be oxidized through treatments, such as aeration (see S3\_Ox).

The mechanism(s) by which the FPW solids form similarly sized Fe/Si particles ( $\sim 200$  nm diameter) could be related to several factors including, the rate of cooling and/or Fe(II) oxidation, high ionic strength, or presence of organic matter (OM). OM is known to alter Fe(II) oxidation rates, control the final mineral formed during mineralization, and in tandem with Si, prevent the ripening of low order iron-oxide species into crystalline forms.<sup>80,81</sup> The incorporation and adsorption of OM by iron-oxides can alter their surface charge preventing aggregation or agglomeration and enhancing their incorporation of contaminants.<sup>82,83</sup>

The second solid phase, a mixed Sr/Ba sulfate, is representative of a barite–celestine solid solution.  $\text{BaSO}_4$  and  $\text{SrSO}_4$  have been found in Marcellus FPW<sup>84</sup> and their solubilities are temperature dependent.<sup>85,86</sup> The Sr/Ba- $\text{SO}_4$  phase likely formed as a function of the FPW cooling from the subsurface to surface temperatures and creating supersaturated conditions that drive their precipitation. Its precipitation is likely rapid, as barite scale formation increases with increasing ionic strength with Na initiating the growth of new step rows; the latter is the rate limiting step in low ionic strength solutions.<sup>87</sup>

### 3.8 Environmental implications

The characterization of FPW solids will enhance the development of new FPW treatment options for reuse, contaminant removal, and transportation risk reductions. To date, the solids have been observed to account for approximately 50% of FPW's PAH load<sup>1,45</sup> and approximately 50% of their total toxicity as measured by  $\text{LC}_{50}$  and EROD.<sup>1,46</sup> Other organic contaminants may also be associated with the solids as only targeted analysis of PAHs have thus far been conducted. As Fe(III) oxyhydroxides were the dominant solid phase, and they are known to adsorb organic contaminants such as PAHs,<sup>88</sup> we hypothesize that majority of PAHs associated with the solids are sorbed to the Fe(III) oxyhydroxides. Furthermore, the fact that the aeration of the FPW generated additional approximately 200 nm diameter Fe/Si particles opposed to resulting in the growth of the previously existing particles is important. These freshly generated Fe/Si particles represent a large increase the particle reactive surface area in the FPW per litre and should enhance the ability of the solids to remove contaminants. Additionally, during simulated hydraulic fracturing experiments with shales containing pyrite and simulated hydraulic fracturing fluids containing dissolved oxygen, Xiong *et al.*<sup>49</sup> observed the generation of hydroxyl radicals and degradation of one HFF chemical, polyacrylamide. They hypothesized that the Fe(II) released by the pyrite in the presence of dissolved oxygen resulted in a free radical chain scission mechanism. Given the wide spread occurrence of presumably Fe(II) in FPW the aeration of FPW to promote the formation of Fe(III) oxyhydroxides by oxidizing residual Fe(II) has the potential to be a widespread treatment technique to remove additional organic contaminants, adsorb or incorporate heavy metals, and reduce the aqueous toxicity of FPW.

While NORMs have not appreciably been found in Duvernay Formation<sup>27</sup> FPW, they are a concern in other formations, such as the Marcellus Formation.<sup>25,26</sup> Ba and Sr sulfates are known to incorporate NORMs such as radium during their formation.<sup>35,89</sup> Therefore, NORMs and their associated risks could be concentrated in the solid phase. Adding sulfate to FPW has been proposed as a treatment to remove Sr and Ba from FPW.<sup>35</sup> Thus, understanding the sources of Ba<sup>56</sup> and removing it from FPW could promote the reuse of FPW by reducing the risk of barite scales.<sup>90</sup> The disposal of these solids, however, would need to account for any NORMs concentrated during treatment.

Additional work will be required to characterize the solids from other basin and understand the mechanisms by which heavy metals, NORMs, and organic contaminants, such as PAHs,<sup>1,45,46</sup> adsorb and desorb from FPW associated solids. This work could be important for remediating FPW spills. Furthermore, treatments that generate iron oxides could remove additional contaminants, reduce the environmental risks associated with FPW, and prevent their formation during the recycling of FPW. These insights will promote the further development of treatment technologies for the reuse of FPW.

## Conflicts of interest

There are no conflicts to declare.

## Acknowledgements

The research presented in this manuscript was funded by Natural Sciences and Engineering Research Council of Canada (NSERC) Collaborative Research and Development (CRD) grant CRDPJ 469308-14 and support from the Encana Corporation to D. S. A., and G. G. G. Special thanks to Dr Gerein at the SEM Laboratory at the University of Alberta and Dr Mukasyan at the Integrated Imaging Facility at the University of Notre Dame for assistance in sample imaging, Dr Jeremy Fein at the University of Notre Dame for facilitating access, and Johanna Weston at Newcastle University for manuscript support. Additionally, we would like to thank the three reviewers for their challenging and helpful suggestions, which aided in the significant improvement of this manuscript.

## References

- 1 Y. He, S. L. Flynn, E. J. Folkerts, Y. Zhang, D. Ruan, D. S. Alessi, J. W. Martin and G. G. Goss, Chemical and toxicological characterization of hydraulic fracturing flowback and produced waters, *Water Res.*, 2017a, **114**, 78–87.
- 2 G. P. Macey, R. Breech, M. Chernaik, C. Cox, D. Larson, D. Thomas and D. O. Carpenter, Air concentrations of volatile compounds near oil and gas production: a community-based exploratory study, *Environ. Health*, 2014, **13**(1), 82.
- 3 R. Davies, G. Foulger, A. Bindley and P. Styles, Induced seismicity and hydraulic fracturing for the recovery of hydrocarbons, *Mar. Pet. Geol.*, 2013, **45**, 171–185.
- 4 K. M. Keranen, M. Weingarten, G. A. Abers, B. A. Bekins and S. Ge, Sharp increase in central Oklahoma seismicity since 2008 induced by massive wastewater injection, *Science*, 2014, **385**, 448–451.
- 5 D. W. Eaton and A. B. Mahani, Focal Mechanisms of Some Inferred Induced Earthquakes in Alberta, Canada, *Seismol. Res. Lett.*, 2015, **86**, 1078–1085.
- 6 S. Goodwin, K. Carlson, K. Knox, C. Douglas and L. Rein, Water intensity assessment of shale gas resources in the Wattenberg Field in Northeastern Colorado, *Environ. Sci. Technol.*, 2014, **48**, 5991–5995.
- 7 A. Kondash and A. Vengosh, Water footprint of hydraulic fracturing, *Environ. Sci. Technol. Lett.*, 2015, **2**, 276–280.
- 8 D. S. Alessi, A. Zolfaghari, S. Kletke, J. Gehman, D. M. Allen and G. G. Goss, Comparative analysis of hydraulic fracturing wastewater practices in unconventional shale development: water sourcing, treatment and disposal practices, *Can. Water Resour. J.*, 2017, **42**, 105–121.
- 9 R. D. Vidic, S. L. Brantley, J. M. Vandenbossche and J. D. Abad, Impact of shale gas development on regional water quality, *Science*, 2013, **340**, 826–835.
- 10 G. T. Llewellyn, F. Dorman, J. L. Westland, D. Yoxtheimer, P. Grieve, T. Sowers, E. H. Fulmer and S. L. Brantley, Evaluating a groundwater supply contamination incident attributed to Marcellus shale gas development, *Proc. Natl. Acad. Sci. U.S.A.*, 2015, **112**, 6325–6330.
- 11 J. B. Jacquet, Review of risks to communities from shale energy development, *Environ. Sci. Technol.*, 2014, **48**, 8321–8333.
- 12 C. D. Kassotis, L. R. Iwanowicz, D. M. Akob, I. M. Cozzarelli, A. C. Mumford, W. H. Orem and S. C. Nagel SC, Endocrine disrupting activities of surface water associated with a West Virginia oil and gas industry wastewater disposal site, *Sci. Total Environ.*, 2016, **557–558**, 901–910.
- 13 E. E. Yost, J. Stanek, R. S. Dewoskin and L. D. Burgoon, Overview of chronic oral toxicity values for chemicals present in hydraulic fracturing fluids, flowback, and produced waters, *Environ. Sci. Technol.*, 2016, **50**, 478–4797.
- 14 N. R. Warner, R. B. Jackson, T. H. Darrah, S. G. Osborn, A. Down, K. Zhao, A. White and A. Vengosh, Geochemical evidence for possible natural migration of Marcellus formation brine to shallow aquifers in Pennsylvania, *Proc. Natl. Acad. Sci. U.S.A.*, 2012, **109**, 11961–11966.
- 15 D. C. DiGuilio and R. B. Jackson, Impact to Underground Sources of Drinking Water and Domestic Wells from Production Well Stimulation and Completion Practices in the Pavilion, Wyoming, Field, *Environ. Sci. Technol.*, 2016, **50**, 4524–4536.
- 16 J. S. Harkness, T. H. Darrah, N. R. Warner, C. J. Whyte, M. T. Moore, R. Millot, W. Kloppman, R. B. Jackson and A. Vengosh, The geochemistry of naturally occurring methane and saline groundwater in an area of unconventional shale gas development, *Geochim. Cosmochim. Acta*, 2017, **208**, 302–334.
- 17 R. B. Jackson, A. Vengosh, W. J. Carey, R. J. Davies, T. H. Darrah, F. O'Sullivan and G. Petron, The

- environmental costs and benefits of fracking, *Annu. Rev. Environ. Resour.*, 2014, **39**, 327–362.
- 18 L. A. Patterson, K. E. Konschnik, H. Wiseman, J. Fargione, K. O. Maloney, J. Kiesecker, J. P. Nicot, S. B. Mordo, S. Entekin, A. Trainor and J. E. Saiers, Unconventional oil and gas spills: risks, mitigation priorities, and state reporting requirements, *Environ. Sci. Technol.*, 2017, **51**, 2563–2573.
  - 19 R. S. Balaba and R. B. Smart, Total arsenic and selenium analysis in Marcellus shale, high-salinity water, and hydrofracture flowback wastewater, *Chemosphere*, 2012, **89**, 1437–1442; E. Barbot, N. S. Vidic, K. B. Gregory and R. D. Vidic, Spatial and temporal correlation of water quality parameters of produced waters from Devonian age shale following hydraulic fracturing, *Environ. Sci. Technol.*, 2013, **47**, 2562–2569.
  - 20 E. Barbot, N. S. Vidic, K. B. Gregory and R. D. Vidic, Spatial and temporal correlation of water quality parameters of produced waters from Devonian age shale following hydraulic fracturing, *Environ. Sci. Technol.*, 2013, **47**, 2562–2569.
  - 21 L. O. Haluszczak, A. W. Rose and L. R. Kump, Geochemical evaluation of flowback brine from Marcellus gas wells in Pennsylvania, USA, *Appl. Geochem.*, 2013, **28**, 55–61.
  - 22 Y. Lester, I. Ferrer, E. M. Thurman, K. A. Sitterly, J. A. Korak, G. Aiken and K. G. Linden, Characterization of hydraulic fracturing flowback water in Colorado: implications for water treatment, *Sci. Total Environ.*, 2015, **512–513**, 637–644.
  - 23 S. Kim, P. O. Ozbek, A. Dhanasekar, A. Prior and K. Carlson, Temporal analysis of flowback and produced water composition from shale oil and gas operations: impact of frac fluid characteristics, *J. Pet. Sci. Eng.*, 2016, **147**, 202–210.
  - 24 A. Zolfaghari, H. Dehghanpour, M. Noel and D. Bearinger, Laboratory and field analysis of flowback water from gas shales, *Journal of Unconventional Oil and Gas Resources*, 2016, **14**, 113–127.
  - 25 S. Almond, S. A. Clancy, R. J. Davies and F. Worrall, The flux of radionuclides in flowback fluid from shale gas exploitation, *Environ. Sci. Pollut. Res.*, 2014, **21**, 12316–12324.
  - 26 A. W. Nelson, D. May, A. W. Knight, E. S. Eitheim, M. Mehroff, R. Shannon, R. Litman and M. K. Schultz, Matrix complications in the determination of radium levels in hydraulic fracturing flowback water from Marcellus shale, *Environ. Sci. Technol. Lett.*, 2014, **1**, 204–208.
  - 27 K. Hoelzer, A. J. Sumner, O. Karatum, R. K. Nelson, B. D. Drollette, M. P. O'Conner, E. L. D'Ambro, G. J. Getzinger, P. L. Ferguson, C. M. Reddy, M. Elsner and D. L. Plata, Indications of transformations products from hydraulic fracturing additives in shale-gas wastewater, *Environ. Sci. Technol.*, 2016, **50**, 8036–8048.
  - 28 D. M. Akob, I. M. Cozzarelli, D. S. Dunlap, E. L. Rowen and M. M. Lorah, Organic and inorganic composition and microbiology of produced waters from Pennsylvania shale gas wells, *Appl. Geochem.*, 2015, **60**, 116–125.
  - 29 K. Oetjen and L. Thomas, Volatile and semi-volatile organic compound patterns in flowback waters from fracturing sites within the Marcellus shale, *Environ. Earth Sci.*, 2016, **75**, 1043.
  - 30 E. M. Thurman, I. Ferrer, J. Blotevogel and T. Borch, Analysis of hydraulic fracturing flowback and produced waters using accurate mass: identification of ethoxylated surfactants, *Anal. Chem.*, 2014, **86**, 9635–9661.
  - 31 K. G. Linden, Hydraulic fracturing wastewater treatment by coagulation-adsorption for removal of organic compounds and turbidity, *J. Environ. Chem. Eng.*, 2016, **4**, 1978–1984.
  - 32 E. M. Thurman, I. Ferrer, J. Rosenblum, K. Linden and J. N. Ryan, Identification of polypropylene glycols and polyethylene glycol carboxylates in flowback and produced water from hydraulic fracturing, *J. Hazard. Mater.*, 2017, **323**, 11–17.
  - 33 I. Ferrer and E. M. Thurman, Analysis of hydraulic fracturing additives by LC/Q-TOF-MS, *Anal. Bioanal. Chem.*, 2015, **407**, 6417–6428.
  - 34 C. He, X. Wang, W. Liu, E. Barbot and R. D. Vidic, Microfiltration in the recycling of Marcellus shale flowback water: solids removal and potential fouling of polymeric microfiltration membranes, *J. Membr. Sci.*, 2014c, **462**, 88–95.
  - 35 C. He, T. Zhang and R. D. Vidic, Co-treatment of abandon mine drainage and Marcellus shale flowback waters for using in hydraulic fracturing, *Water Res.*, 2016, **104**, 425–431.
  - 36 B. Xiong, A. L. Zydney and M. Kumar, Fouling of microfiltration membranes by flowback and produced waters from the Marcellus shale gas play, *Water Res.*, 2016, **99**, 162–170.
  - 37 G. Li, B. Bai and K. H. Carlson, Characterization of solids in produced water from wells fracturing with recycled and fresh water, *J. Pet. Sci. Eng.*, 2016, **114**, 91–98.
  - 38 T. T. Phan, J. A. Hakala and D. J. Bain, Influence of colloids on metal concentrations and radiogenic strontium isotopes in groundwater and oil and gas-produced waters, *Appl. Geochem.*, 2018, **95**, 85–96.
  - 39 M. C. Graham, I. W. Oliver, A. B. Mackenzie, R. M. Ellam and J. G. Farmer, Mechanisms controlling lateral and vertical porewater migration of depleted uranium (DU) at two UK weapons testing sites, *Sci. Total Environ.*, 2011, **409**, 1854–1866.
  - 40 Y. Wang, M. Fruttschi, E. Suvorova, V. Phrommavanh, M. Descostes, A. A. A. Osman, G. Geipel and R. Bernier-Latmani, Mobile uranium(IV)-bearing colloids in a mining impacted wetland, *Nat. Commun.*, 2013, **4**, 2942.
  - 41 A. B. Kersting, D. W. Efurud, D. L. Finnegan, D. J. Rokop, D. K. Smith and J. L. Thompson, Migration of plutonium in ground water at the Nevada Test Site, *Nature*, 1999, **397**, 56–59.
  - 42 A. P. Novikov, S. N. Kalmykov, S. Utsunomiya, R. C. Ewing, F. Horreard, A. Merkulov, S. B. Clark, V. V. Tkachev and B. F. Myasoedov, Colloid transport of plutonium in the far-field of Mayak production association, Russia, *Science*, 2006, **314**, 638–641.
  - 43 D. A. Backhus, J. N. Ryan, D. M. Groher, J. K. MacFarlane and P. M. Gschwend, Sampling colloids and colloid-associated

- contaminants in ground water, *Groundwater*, 1993, **31**, 466–479.
- 44 A. A. Mackay and P. M. Gschwend, Enhanced concentrations of PAHs in groundwater at a coal tar site, *Environ. Sci. Technol.*, 2001, **35**, 1320–1328.
- 45 Y. He, E. J. Folkerts, Y. Zhang, J. W. Martin, D. S. Alessi and G. G. Goss, Effects on biotransformation, oxidative stress, and endocrine disruption in rainbow trout (*Oncorhynchus mykiss*) exposed to hydraulic fracturing flowback and produced waters, *Environ. Sci. Technol.*, 2017b, **51**, 940–947.
- 46 Y. He, C. Sun, E. J. Folkerts, J. W. Martin and G. G. Goss, Developmental toxicity of the organic fraction from hydraulically fractured flowback and produced waters to early life stages of zebrafish (*Danio rerio*), *Environ. Sci. Technol.*, 2018, **52**, 3820–3830.
- 47 S. D. A. Anderson, C. D. Rokosh, J. G. Pawlowicz, H. Berhane and A. P. Beaton, *Mineralogy, permeametry, mercury porosimetry, pycnometry and scanning electron microscope imaging of Duvernay and Muskwa Formations in Alberta: Shale Gas Data Release: ERCB/AGS Open File 830 Report*, 2010, [https://ags.aer.ca/document/OFR/OFR\\_2010\\_02.pdf](https://ags.aer.ca/document/OFR/OFR_2010_02.pdf), accessed November 2018.
- 48 M. R. Yassin, M. Begum and H. Dehghanpour, Organic shale wettability and its relationship to other petrophysical properties: a Duvernay case study, *Int. J. Coal Geol.*, 2017, **169**, 74–91.
- 49 B. Xiong, Z. Miller, S. Roman-White, T. Tasker, B. Farina, B. Piechowicz, W. D. Burgos, P. Joshi, L. Zhu, C. A. Gorski and A. L. Zydney, Chemical Degradation of Polyacrylamide during Hydraulic Fracturing, *Environ. Sci. Technol.*, 2017, **52**, 327–336.
- 50 T. A. Blewett, P. L. M. Delompre, Y. He, E. J. Folkerts, S. L. Flynn, D. S. Alessi and G. G. Goss, Sublethal and reproductive effects of acute and chronic exposure to flowback and produced water from hydraulic fracturing on the water flea *Daphnia magna*, *Environ. Sci. Technol.*, 2017, **51**, 3032–3039.
- 51 GBC Scientific Equipment, *The determination of aluminum, iron and silicon in rock samples*, [http://www.gbcscientific.com/appnotes/AA\\_app\\_note\\_001.pdf](http://www.gbcscientific.com/appnotes/AA_app_note_001.pdf), accessed May 2016.
- 52 K. von Gunten, M. S. Alam, M. Hubmann, Y. S. Ok, K. O. Konhauser and D. S. Alessi, Modified sequential extraction for biochar and petroleum coke: metal release potential and its environmental implications, *Bioresour. Technol.*, 2017, **236**, 106–110.
- 53 K. Porsch and A. Kappler, Fe(II) oxidation by molecular O<sub>2</sub> during HCl extraction, *Environ. Chem.*, 2011, **8**, 190–197.
- 54 J. V. Walther and H. C. Helgeson, Calculation of the thermodynamic properties of aqueous silica and the solubility of quartz and its polymorphs at high pressure and temperature, *Am. J. Sci.*, 1977, **277**, 241–251.
- 55 C. T. Chen and W. L. Marshall, Amorphous silica solubilities IV. Behavior in pure water and aqueous sodium chloride, magnesium chloride, sodium sulfate, magnesium chloride, and magnesium sulfate solutions up to 350 C, *Geochim. Cosmochim. Acta*, 1982, **46**, 279–297.
- 56 D. Renock, J. D. Landis and M. Sharma, Reductive weathering of black shale and release of barium during hydraulic fracturing, *Appl. Geochem.*, 2016, **65**, 73–86.
- 57 P. Bennett and D. I. Siegel, Increasing solubility of quartz in water due to complexing by organic compounds, *Nature*, 1987, **326**, 684–686.
- 58 P. Bennett, Quartz dissolution in organic-rich aqueous systems, *Geochim. Cosmochim. Acta*, 1991, **55**, 1781–1797.
- 59 A. D. Jew, M. K. Dustin, A. L. Harrison, C. M. J. Wong, D. L. Thomas, K. Maher, G. E. Brown and J. R. Bargar, Impact of organics and carbonates on the oxidation and precipitation of iron during hydraulic fracturing of shale, *Energy Fuels*, 2017, **31**, 3643–3658.
- 60 M. Xu, M. Binazadeh, A. Zolfaghari and H. Dehghanpour, Effects of dissolved oxygen on water imbibition in gas shales, *Energy Fuels*, 2018, **32**, 4695–4704.
- 61 N. Abualfaraj, P. L. Gurian and M. S. Olson, Characterization of Marcellus Shale Flowback Water, *Environ. Eng. Sci.*, 2014, **31**, 514–524.
- 62 N. Shrestha, G. Chilkoor, J. Wilder, V. Gadhamshetty and J. J. Stone, Potential water resource impacts of hydraulic fracturing from unconventional oil production in the Bakken shale, *Water Res.*, 2017, **108**, 1–24.
- 63 A. Shramko, T. Palmgren, D. Gallo, and R. Dicit, Analytical characterization of flowback waters in the field, *16<sup>th</sup> Annual Petroleum and Biofuels Environmental Conference*, IPEC, Houston, November 3–5, 2009.
- 64 *Environment Agency Report: Shale gas north west—monitoring of flow back water*, [http://webarchive.nationalarchives.gov.uk/20140328145127/http://www.environment-agency.gov.uk/static/documents/Business/6th\\_Dec\\_-\\_Shale\\_gas\\_-\\_North\\_West\\_-\\_Monitoring\\_of\\_flowback\\_water\\_-\\_update\\_\(3\).pdf](http://webarchive.nationalarchives.gov.uk/20140328145127/http://www.environment-agency.gov.uk/static/documents/Business/6th_Dec_-_Shale_gas_-_North_West_-_Monitoring_of_flowback_water_-_update_(3).pdf), accessed October 2017.
- 65 T. L. Tasker, W. D. Burgos, P. Piotrowski, L. Castillo-Meza, T. A. Blewett, K. B. Ganow, A. Stallworth, P. L. Delompre, G. G. Goss, L. B. Fowler and J. P. Vanden Heuvel, Environmental and Human Health Impacts of Spreading Oil and Gas Wastewater on Roads, *Environ. Sci. Technol.*, 2018, **52**, 7081–7091.
- 66 M. G. Fowler, L. D. Stasiuk, M. Hearn and M. Obermajer, Devonian hydrocarbon source rocks and their derived oils in the Western Canada Sedimentary Basin, *Bull. Can. Pet. Geol.*, 2001, **49**, 117–148.
- 67 S. E. Arthur, P. V. Brady, R. T. Cygan, H. L. Anderson and H. E. Westrich, Irreversible sorption of contaminants during ferrihydrite transformation, *Proceedings of the Waste Management Conference, WM*, 1999, vol. 99, pp. 1–14.
- 68 R. S. Taylor, B. Stobo, G. Niebergall, R. Aguilera, J. Walter and E. Hards, Optimization of Duvernay fracturing treatment design using fully compositional dual permeability numeric reservoir simulation, *SPE/CSUR Unconventional Resources Conference*, Society of Petroleum Engineers, Canada, September 30, 2014.
- 69 D. Parkhurst and C. A. J. Appelo, *PHREEQC (Version 3)-A Computer Program for Speciation, Batch-Reaction, One-Dimensional Transport, and Inverse Geochemical*

- Calculations*, US Geologic Survey, Water Resources Division, Denver, CO, 2013.
- 70 A. E. Booker, M. A. Borton, R. A. Daly, S. A. Welch, C. D. Nicora, D. W. Hoyt, T. Wilson, S. O. Purvine, R. A. Wolfe, S. Sharma and P. J. Mouser, Sulfide generation by dominant *Halanaerobium* microorganisms in hydraulically fractured shales, *mSphere*, 2017, 2(4), e00257-17.
- 71 N. R. Warner, T. M. Kresse, P. D. Hays, A. Down, J. D. Karr, R. B. Jackson and A. Vengosh, Geochemical and isotopic variations in shallow groundwater in areas of the Fayetteville shale development, north-central Arkansas, *Appl. Geochem.*, 2013, 35, 207–220.
- 72 T. Hayes and B. F. Severin, *Barnett and Appalachian shale water management and reuse technologies*, Report No. 08122-05, Research partnership to secure energy for America, 2012, [https://edx.netl.doe.gov/dataset/barnett-and-appalachian-shale-water-management-and-reuse-technologies/resource\\_download/d167805d-9a16-40b8-b3fb-123ac3edab20](https://edx.netl.doe.gov/dataset/barnett-and-appalachian-shale-water-management-and-reuse-technologies/resource_download/d167805d-9a16-40b8-b3fb-123ac3edab20), accessed November 2018.
- 73 J. S. Rosenblum, K. A. Sitterley, E. M. Thurman, I. Ferrer and K. G. Linden, Hydraulic fracturing wastewater treatment by coagulation-adsorption for removal of organic compounds and turbidity, *J. Environ. Chem. Eng.*, 2016, 4(2), 1978–1984.
- 74 J. Webster, *Haynesville Shale*, American Association of Drilling Engineers, Chesapeake Energy, 2009, <http://www.aade.org/app/download/7021874804/AADE+-Haynesville+Shale+Drilling+%28Chesapeake%29.pdf>, accessed November 2018.
- 75 L. Wang, Z. Dong and Z. Xia, A multi-scale flow model for production performance analysis in shale gas reservoirs with fractal geometry, *Sci. Rep.*, 2018, 8(1), 11464.
- 76 O. O. Adekunle and B. T. Hoffman, Minimum Miscibility Pressure Studies in the Bakken, in *SPE Improved Oil Recovery Symposium*, Society of Petroleum Engineers, 2014.
- 77 P. H. Nelson and S. L. Santus, Gas, oil, and water production from Wattenberg field in the Denver Basin, Colorado, *US Geological Survey Open-File Report*, 2011-1175, 2011.
- 78 S. K. Juniper and Y. Fouquet, Filamentous iron-silica deposits from modern and ancient hydrothermal sites, *Can. Mineral.*, 1988, 26, 859–869.
- 79 K. O. Konhauser and F. G. Ferris, Diversity of iron and silica precipitation by microbial mats in hydrothermal waters, Iceland: implications for precambrian iron formations, *Geology*, 1996, 24, 323–326.
- 80 R. M. Cornell and U. Schwertmann, Influence of organic anions on the crystallization of ferrihydrite, *Clays Clay Miner.*, 1979, 27, 402–410.
- 81 A. M. Jones, R. N. Collins, J. Rose and T. D. Waite, The effect of silica and natural organic matter on the Fe(II)-catalysed transformation and reactivity of Fe(II) minerals, *Geochim. Cosmochim. Acta*, 2009, 73, 4409–4422.
- 82 D. Perret, J. F. Gaillard, J. Dominik and O. Atteia, The diversity of natural hydrous iron oxides, *Environ. Sci. Technol.*, 2014, 34, 3540–3546.
- 83 K. Eusterhues, T. Rennert, H. Knicker, I. Kogel-Knabner, K. U. Totsche and U. Schwertmann, Fractionation of organic matter due to reaction with ferrihydrite: coprecipitation versus adsorption, *Environ. Sci. Technol.*, 2011, 45, 527–533.
- 84 C. He and R. D. Vidic, Impact of antiscalants on the fate of barite in the unconventional gas wells, *Environ. Eng. Sci.*, 2014b, 33, 745–752.
- 85 C. W. Blout, Barite solubilities and thermodynamic qualities up to 300 °C and 1400 bars, *Am. Mineral.*, 1977, 62, 942–957.
- 86 B. Y. Zhen-Wu, K. Dideriksen, J. Olsson, P. J. Raahauge, S. L. S. Stipp and E. H. Oelkers, Experimental determination of barite dissolution and precipitations rates as a function of temperature and aqueous fluid composition, *Geochim. Cosmochim. Acta*, 2016, 194, 193–210.
- 87 P. Risthaus, D. Bosbach, U. Becker and A. Putnis, Barite scale formation and dissolution at high ionic strength studied with atomic force microscopy, *Colloids Surf.*, 2001, 191, 201–214.
- 88 K. Nielson, Y. Kalmykova, A. M. Stromvall, B. Anders and E. Eriksson, Particle phase distribution of polycyclic aromatic hydrocarbons in stormwater- using humic acid and iron nano-sized colloids as test particles, *Sci. Total Environ.*, 2015, 532, 103–111.
- 89 A. Kondash, N. R. Warner, O. Lahav and A. Vengosh, Radium and barium removal through blending hydraulic fracturing fluids with acid mine drainage, *Environ. Sci. Technol.*, 2014, 48, 1334–1342.
- 90 C. He, M. Li, W. Liu, E. Barbot and R. D. Vidic, Kinetics and equilibrium of barium and strontium sulfate formation in Marcellus shale flowback water, *J. Environ. Eng.*, 2013, 140, B4014001.